Kinetic Modelling of Electroless Nickel–Phosphorus Plating under High Pressure

Aurélie Galfré, Hirotaka Yokohama, Mélaz Tayakout-Fayolle, Naoki Fukumuro, Shinji Yae, Kouji Maeda, Takuji Yamamoto

ACS OMEGA

http://pubs.acs.org/journal/acsodf

Article

Kinetic Modelling of Electroless Nickel–Phosphorus Plating under High Pressure

Hirotaka Yokohama, Mélaz Tayakout-Fayolle, Aurélie Galfré, Naoki Fukumuro, Shinji Yae, Kouji Maeda, and Takuji Yamamoto*

Cite This: *ACS Omega* 2020, 5, 6937–6946

Read Online

ACCESS | Metrics & More | Article Recommendations

ABSTRACT: In electroless nickel–phosphorus plating (ENPP), growth of the plated layer under high pressure was found to be faster than under ambient pressure. To quantitatively elucidate the effect of high pressure on the mechanism of the ENPP reaction, we propose a kinetic model that takes into account both mass transfer and reaction of the chemical species present in the plating solution. We solved the mass balance equations between the chemical species to calculate the transient changes in the thickness of the plated layer as well as the concentrations of the chemical species in the plating solution. By fitting the calculated results to the experimentally acquired results based on the nonlinear least square method, we determined such parameters as the film mass transfer coefficient, the adsorption constants, and the reaction rate constants of the chemical species in the model. As a result, we found that the film mass transfer coefficient under high pressure was greater than that under ambient pressure and revealed the dependence of the coefficient on pressure. The transient changes in the concentrations of the chemical species in the plating solution that we calculated based on the kinetic model employing our estimated parameters closely modeled the experimental results with the determination coefficients being mostly over 99%.

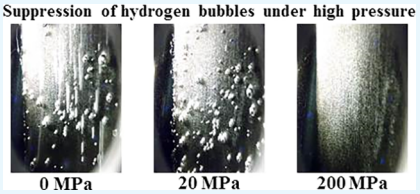

1. INTRODUCTION

New developments in the science and technology of high pressure are increasingly being applied to industrial processes such as isostatic pressing, hydrothermal synthesis, and pressure crystallization. Isostatic pressing is a molding method that produces densely compacted and crystallized ceramics or metals in industrial alloy fabrication.[1] Li et al. employed isostatic pressing followed by plastic extrusion to prepare tubular-type membranes composed of densely compacted perovskite.[2] The carbon and graphite industry has developed high-pressure molding techniques at elevated temperatures to obtain homogeneous and refined graphite materials to use as arc light electrodes.[3] As recently reviewed by Bazargan et al.,[4] high-pressure techniques have the potential to produce novel carbon materials, such as spheres, prolate spheroids, and nanotubes with varying morphologies and physical properties. Hydrothermal syntheses of porous solids with periodic mesostructures were recently reviewed by Mandal and Landskron.[5] Nanocasting under high pressure is an efficient method that enables the preservation of periodic mesostructures during the liquid-to-solid phase transformation of the starting materials. Li et al. employed Raman spectroscopy in an in situ study on the solubility of ionic liquids in methanol under pressures of up to 2 GPa.[6] They reported the coexistence of two different crystalline phases of the ionic liquids. In the crystallization of amorphous calcium carbonate (ACC) under pressures of up to 640 MPa, the water content as well as the crystallinity of the prepared ACC solids depends on the added pressure.[7] Moritoki et al. summarized the features of high-pressure crystallization processes in industrial processes.[8] They reported that pressure is the driving parameter not only for crystallization but also for separation and purification of individual components from a mixture.

Electroless plating is a useful technique for forming a metal-plated layer on the surface of various solids, including nonconductors such as ceramics or plastics, without employing an external power source.[9−11] It is an autocatalytic chemical deposition method in the sense that the deposited metal is catalytically responsive to the oxidation reaction of a reducing agent, which leads to the continuous growth of the plated layer. A plated layer with the desired thickness can easily be formed, even on surfaces with complicated shapes, by controlling, for example, the plating time. Brenner and Riddel developed a practical electroless nickel plating method as a result of their discovery that hypophosphite can reduce the ionic form of nickel species to their metallic form.[12] In contrast to conventional reducing agents such as tetrahydroborate or dimethylaminebor-

Received: January 22, 2020
Accepted: March 9, 2020
Published: March 20, 2020

https://dx.doi.org/10.1021/acsomega.0c00312
ACS Omega 2020, 5, 6937–6946

ane, hypophosphite is inexpensive and is stable in the plating solution. Of the different types of electroless plating methods, electroless nickel−phosphorus plating (ENPP)[13,14] has the advantages of corrosion resistance as well as a fast deposition rate. ENPP is increasingly applied industrially in the manufacture of automobiles, electronic devices, and precision instruments. The conditions for ENPP are being intensively studied to further improve the cost efficiency and characteristics of the plated layer.[15,16] Although it is possible to control the thickness of the plated layer by changing the operating conditions such as time, temperature, and stirring rate in the plating bath, the key aim is to form a plated layer that is free from defects. The oxidation reaction of a reducing agent, which is employed in ENPP to supply electrons for the reduction of metal ion species in a plating solution, is accompanied by the evolution of hydrogen. In the ENPP process under ambient pressure, hydrogen bubbles are generated on the surface of the plated layer during the oxidation reaction of the reducing agent, sometimes resulting in roughness of or defects in the plated layer. On the other hand, if ENPP is performed under high pressure, the hydrogen generated by the plating reaction instead dissolves in the plating solution. As a consequence, hydrogen bubbles, which inhibit the mass transfer of the chemical species involved in the plating reaction from the plating solution to the plated surface, are not formed. In a previous study, we confirmed that the average plating rate under an elevated pressure of 20 MPa was about 1.5 times faster than that under ambient pressure.[17] High pressure was also found effective to form a smoother plated surface layer. The result might be also attributed to the equilibrium shift in the reaction to generate hydrogen ($2H^+ + 2e^- \Leftrightarrow H_2$) from right to left. However, to date, little has been known of the mechanism of the plating reaction under high pressure or of the effects that high pressure has on the plating reaction. Kinetic modeling of the reaction, however, is a promising and useful method for revealing the effects of high pressure on the mass transfer of the chemical species in the plating solution as well as the formation of the plated surface.

In various chemical reactions, kinetic modeling has been applied to quantitatively evaluate the effects of operating conditions on the reaction mechanism. Nguyen et al. employed the Langmuir−Hinshelwood model, which considers both liquid−vapor mass transfer and competitive adsorption of the reactants, products, and solvents on γ-Al_2O_3 or amorphous silica−alumina-supported NiMo catalysts to gain an understanding of the hydrodenitrogenation of quinoline in a batch reactor. Kinetic modeling of the reaction revealed the hydrogenation of 1,2,3,4-tetrahydroquinoline into decahydroquinoline to be the rate-determining step in the principal reaction pathway.[18] In a mass transport process of toxic chemical vapors employing an activated carbon fiber cloth, Lordgooei et al. considered the effective diffusivities in the adsorbents as a function of temperature, the concentration, and the pore size distribution to build a dispersive computational model for industrial applications.[19] For a system of water droplets dispersed in oil containing the synthetic surfactants tetracarboxylic acid (BP10) and decanoic acid (DA), Kovalchuc et al. built a multicomponent mass transport model to determine the interfacial composition and bulk phase concentration of the surfactants. By employing a molecular-mixed monolayer adsorption model that was parameterized in molecular dynamic simulation and interfacial tension experiments, they revealed that the interfacial composition of BP10 and DA closely depended on the surface-to-volume ratio of the system.[20]

In this study, we aim to clarify the effects of high pressure on ENPP. To solve the mass balance equations of the chemical species involved in the ENPP reaction, we propose a kinetic model considering both mass transfer and the reactions of the chemical species in a plating solution. By comparing the results that we numerically calculate based on the model with the experimental data, we determine such parameters in the model as the film mass transfer coefficient of the chemical species on the growing surface of the plated layer, the adsorption constants, and the reaction rate constants. We then discuss the effect of the pressure on the reaction mechanism of the ENPP and the quality of the plated layer.

2. EXPERIMENTAL SECTION

2.1. Electroless Nickel−Phosphorus Plating. Figure 1 shows a schematic image of the high-pressure apparatus employed in this study. First, a degreased and pickled copper piece, 10 mm wide and 20 mm high, with the thickness of 0.3 mm was placed in a tubular glass cell with 3 mL of a plating solution that contained the chemical species listed in Table 1.

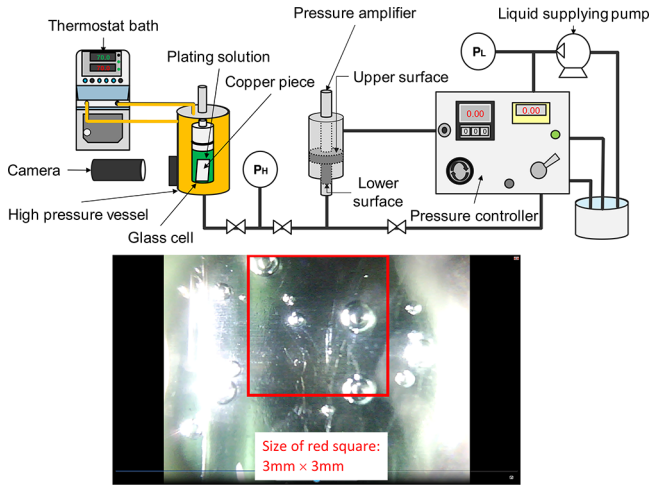

Figure 1. Schematic image of the high-pressure apparatus and an image of hydrogen bubbles on the surface of a copper piece under atmospheric pressure (P = 0 MPa).

Table 1. Composition of the Plating Solution

chemical species	formula weight (−)	molar concentration (kmol·m^{-3})
sodium succinate hexahydrate	270.14	0.10
DL-malic acid	134.09	0.10
nickel(II) sulfate hexahydrate	262.85	0.10
sodium phosphinate monohydrate	105.99	0.30
sodium saccharin dihydrate	241.20	0.0060

The effective surface-to-volume ratio, a, of the copper piece is estimated to be 6.67×10^3 m^2·m^{-3}, based on the surface area (4.0×10^{-4} m^2) considering its both sides and the volume (6.0×10^{-8} m^3.) The cell was placed in the high-pressure vessel, which was then pressurized employing a liquid supplying pump with a syringe-type pressure amplifier. As depicted in Figure 1, the area of the upper surface of the cylinder in the pressure amplifier was 20 times as great as that of the lower surface. The pressure added by the pump was multiplied 20-fold using the pressure amplifier

https://dx.doi.org/10.1021/acsomega.0c00312
ACS Omega 2020, 5, 6937−6946

to achieve the desired pressure P which we varied from 0 to 200 MPa. P indicates the pressure added to the vessel before elevating the temperature. To initiate the plating reaction, the solution was heated to 343 K by circulating hot water between the thermostat bath and high-pressure vessel. By elevating the temperature, the pressure inside the vessel increased to a certain extent. The plated layer, composed of metallic nickel and nickel−phosphorus alloy, was then deposited on both surfaces of the piece. We varied the reaction time from 600 to 4800 s. The reaction was terminated by cooling the high-pressure vessel to 298 K. The pressure inside the vessel was then gradually decreased to ambient pressure. Under atmospheric pressure (P = 0 MPa), generation of hydrogen bubbles could be observed on the surface of a copper piece. The size and number of the bubbles on the surface were measured employing a pen-type camera (CJK-01, MK Electronics Corp.). Under the other pressure examined in this study, we observed no bubbles on the copper piece.

Finally, we measured the increase in the mass of the piece subjected to the plating reaction to determine the average thickness, δ, of the plated layer according to the following eq 1

$$\delta = \frac{(M_1 - M_2)}{A \times \rho} \times 10^6 \quad (1)$$

where M_1, M_2, A, and ρ are the weight of copper piece after plating, the weight of copper piece before plating, the surface area (4.0×10^{-4} m^2) of a copper piece of both sides, and the average density (7.63×10^3 kg·m^{-3}) of the plated layer, respectively.

2.2. Chemical Reactions in Electroless Nickel−Phosphorus Plating. In a typical electroless plating process, small catalytic sites must be introduced onto the substrate prior to the reaction to serve as nuclei for the plated layer growth.[21] To initiate the plating reaction, we employ a cylindrical aluminum stick with a length of 100 mm and a diameter of 3 mm as the trigger to initiate the plating reaction. The electroless plating reaction is driven by the ionization tendency of the relevant metal species. In the case of this study, by attaching the aluminum stick to the surface of the copper piece, aluminum is ionized to supply electrons to noble metal, nickel. Eqs 2−5 are elementary reactions with regard to the deposition of the plated layer. Initially, electrons generated by the oxidation of metallic aluminum reduce nickel cations to metallic nickel, which acts as a catalyst for the further reduction of nickel cations. Thus, the reduction of the nickel cation is an autocatalytic reaction. Then, as expressed by eq 2, the hypophosphite anion is reduced to a phosphite anion and supplies electrons. As a result, the reactions expressed by eqs 3−5 proceed simultaneously. The plated layer deposited on the copper piece is an alloy composed of Ni and Ni_2P. As the reaction progresses under ambient pressure, hydrogen is evolved and forms bubbles on the surface of the plated layerreaction in the liquid phase

$$H_2PO_2^- + H_2O \rightarrow H_2PO_3^- + 2H^+ + 2e^- \quad (2)$$

reaction at the surface of copper

$$Ni^{2+} + 2e^- \rightarrow Ni \quad (3)$$

$$2Ni^{2+} + H_2PO_2^- + 2H^+ + 5e^- \rightarrow Ni_2P + 2H_2O \quad (4)$$

$$2H^+ + 2e^- \rightarrow H_2 \quad (5)$$

2.3. Quantitative Analysis of Chemical Species. The concentrations of both hypophosphite ($H_2PO_2^-$) and phosphite ($H_2PO_3^-$) anions in the plating solution were measured employing an ion chromatograph equipped with an electric conductivity detector (Model IA-100, DKK-TOA Corp) and an anion exchange column (Model I-524A, Showa Denko K.K.) at 313 K. The eluent was 0.001 mol·dm^{-3} DL-tartaric acid. The measurement was performed at intervals of 15 min under a constant eluent flow of 5.35 mL·min^{-1}. The concentration of each anion was determined based on a calibration curve that was plotted using sodium phosphinate monohydrate for $H_2PO_2^-$ and disodium hydrogen phosphite pentahydrate for $H_2PO_3^-$, respectively. The concentration of the residual nickel cation was determined from the mass and the phosphorus content of the plated layer. The phosphorus content of the plated layer was determined to be 12% as a result of measurements by energy-dispersive X-ray spectroscopy (EDX).

3. KINETIC MODELING

3.1. Mass Transfer at the Solid−Liquid Interface (SLI). As depicted in Figure 2, a kinetic model was built to account for

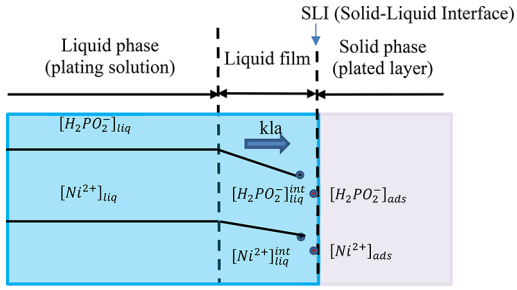

Figure 2. Schematic image of mass transfer around the SLI.

the mass transfer of the chemical species in the vicinity of the SLI, which was the growing surface of the plated layer formed on the surface of the copper piece. The kinetic parameters employed in the model are summarized in Table 2.

Table 2. Kinetic Parameters Considered in the Model

kla (s^{-1})	volumetric mass transfer coefficient of the chemical species in the liquid film
K_{ad1} (−)	adsorption constant of $H_2PO_2^-$ on SLI
K_{ad2} (−)	adsorption constant of Ni^{2+} on SLI
k_1 (s^{-1})	reaction rate constant of eq 2
k_2 (s^{-1})	reaction rate constant of eq 3
k_3 (dm^6·mol^{-2}·s^{-1})	reaction rate constant of eq 4

3.2. Assumptions. The mass balances of the cation and anion species were considered based on the following general and transport assumptions

(1) General assumptions
  (i) The plating solution in the cell is homogeneous. In the case of atmospheric pressure (P = 0 MPa), the volume of generated hydrogen gas (2 vol % max.) can be neglected compared to that of the plating solution.
  (ii) All surface areas of the copper piece contribute to adsorption and reaction of the chemical species except for the case under atmospheric pressure (P = 0 MPa). In the said case, the generation of hydrogen bubbles on the piece results in the decrease of the available surface area for mass

https://dx.doi.org/10.1021/acsomega.0c00312
ACS Omega 2020, 5, 6937−6946

transfer of the species. The ratio (13%) of the decreased available area which we determined by observing the bubbles to the total surface areas of the piece is taken into account by correcting *kla* with the ratio.

(iii) The volume and temperature of the solution are constant.

(iv) The linear adsorption model with the constant K_{ad} is employed to account for the distributions of both $H_2PO_2^-$ and Ni^{2+} at the SLI as expressed by the eqs 6 and 7, while $H_2PO_3^-$ does not adsorb onto the SLI.

$$[H_2PO_2^-]_{liq}^{int} = K_{ad1}\cdot[H_2PO_2^-]_{ads} \quad (6)$$

$$[Ni^{2+}]_{liq}^{int} = K_{ad2}\cdot[Ni^{2+}]_{ads} \quad (7)$$

(v) The density of the plated layer is constant, irrespective of its thickness, and is equal to 7.63 g·cm^{-3}, which is calculated from the atomic ratio between phosphorus and nickel based on the results of energy-dispersive X-ray analysis.

(2) Transport assumptions

The molar flux of an ionic species in a dilute solution is composed of two terms, one corresponding to the molar diffusion according to Fick's law and the other to the electrophoretic migration.[22] The second term is equal to zero if the electrical charge density is equal to zero.[22] The charge densities of cations and anions in the plating solution versus time were calculated from eqs 8 and 9, respectively, under the condition of P = 30 MPa. The values are presented in Figure 3.

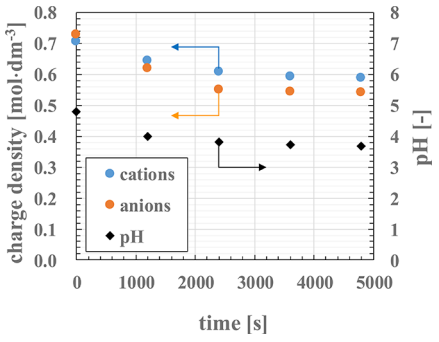

Figure 3. Transient changes of charge density of cations and anions in the plating solution.

Cation charge density

$$[Na^+]_{liq} + 2[Ni^{2+}]_{liq} + [H^+]_{liq} \quad (8)$$

Anion charge density

$$[C_7H_3NO_3S^-]_{liq} + [C_4H_3O_4^-]_{liq} + 2[C_4H_2O_4^{2-}]_{liq} + [C_4H_3O_5^-]_{liq} + 2[C_4H_2O_5^{2-}]_{liq} + [H_2PO_2^-]liq + [H_2PO_3^-]_{liq} + 2[SO_4^{2-}]_{liq} \quad (9)$$

In eqs 8 and 9, the concentrations of each ionic species, except for spectator ions (Na^+, SO_4^{2-}), vary according to the chemical reactions expressed by eqs 3−5 and the dissociation equilibria of the plating solution additives.[23]

The dissociation equilibrium of each additive in the plating solution is summarized in Table 3.[23] In Figure 3, the transient changes of the charge density of cations and anions are almost the same, although a small discrepancy between the results is observed from 1200 s. Hence, as the first approximation, the electrical charge density of the solution can be considered to be almost zero during the plating reaction. The assumption (i) can be formulated.

Table 3. Acidity Constant and Dissociation Equilibrium of the Plating Solution Additives[23]

chemical species	acidity constant (25 °C)	dissociation equilibrium
sodium succinate hexahydrate (SH_2)	4.2 (pK_{a1}), 5.6 (pK_{a2})	$SH_2 \leftrightarrow SH^- + H^+$ $SH^- \leftrightarrow S^{2-} + H^+$
DL-malic acid (MH_2)	3.5 (pK_{a1}), 5.1 (pK_{a2})	$MH_2 \leftrightarrow MH^- + H^+$ $MH^- \leftrightarrow M^{2-} + H^+$
sodium saccharin (AH)	1.6	$AH \leftrightarrow A^- + H^+$

(i) A linear driving force (LDF) approximation is adequate to represent the transfer of ionic species in the vicinity of the plated layer under the conditions examined in this study.

(ii) *kla* is the only parameter that depends on pressure. The other parameters (K_{ad1}, K_{ad2}, k_1, k_2, and k_3) are independent of it.

(iii) The volumetric mass transfer coefficient, *kla*, in the liquid film is assumed to be the same for $H_2PO_2^-$ and Ni^{2+} based on the relation between the two diffusion coefficients,[24,25] as follows

$$\frac{D_{Ni^{2+}}}{D_{H_2PO_2^-}} = \frac{\lambda_{Ni^{2+}}}{\lambda_{H_2PO_2^-}}\frac{z_{H_2PO_2^-}}{z_{Ni^{2+}}} \approx 1 \quad (10)$$

3.3. Mass Balance Equations. Based on the model and assumptions explained in the previous sections, the mass balances between the cation and anion species contained in the plating solution can be expressed by the following eqs 11−17

Mass balances for the liquid phase

$$\frac{d[H_2PO_2^-]_{liq}}{dt} = -kla\cdot\frac{V_{sol}}{V_{liq}}\cdot([H_2PO_2^-]_{liq} - K_{ad1}\cdot[H_2PO_2^-]_{ads}) - k_1\cdot[H_2PO_2^-]_{liq} \quad (11)$$

$$\frac{d[Ni^{2+}]_{liq}}{dt} = -kla\cdot\frac{V_{sol}}{V_{liq}}\cdot([Ni^{2+}]_{liq} - K_{ad2}\cdot[Ni^{2+}]_{ads}) \quad (12)$$

$$\frac{d[H_2PO_3^-]_{liq}}{dt} = k_1\cdot[H_2PO_2^-]_{liq} \quad (13)$$

Mass balances on the solid phase

$$\frac{d[H_2PO_2^-]_{ads}}{dt} = kla\cdot([H_2PO_2^-]_{liq} - K_{ad1}\cdot[H_2PO_2^-]_{ads}) - k_3\cdot[H_2PO_2^-]_{ads}\,[Ni^{2+}]_{ads}^2 \quad (14)$$

$$\frac{d[Ni^{2+}]_{ads}}{dt} = kla\cdot([Ni^{2+}]_{liq} - K_{ad2}\cdot[Ni^{2+}]_{ads}) - k_2\cdot[Ni^{2+}]_{ads} - 2\cdot k_3\cdot[H_2PO_2^-]_{ads}\,[Ni^{2+}]_{ads}^2 \quad (15)$$

https://dx.doi.org/10.1021/acsomega.0c00312
ACS Omega 2020, 5, 6937−6946

Table 4. Value and Uncertainty Interval of the Parameters Estimated under the Condition of P = 30 MPa

parameter	kla (s^{-1})	K_{ad1} (−)	K_{ad2} (−)	k_1 (s^{-1})	k_2 (s^{-1})	k_3 ($dm^6 \cdot mol^{-2} \cdot s^{-1}$)
value	13.96	0.006613	0.1431	0.0004657	4.057	1.098
ui[a]	0.1563	0.004932	0.1224	0.0001213	0.3675	0.1814
error[b]	1.120	74.58	85.51	26.05	9.059	16.52

[a]Uncertainty interval in the numerical estimation of kla. [b]The percentage of ui to the estimated kla value.

Table 5. Value and Uncertainty Interval of kla under the Different Conditions of P

P (MPa)	0	30	50	100	150	200
kla (s^{-1})	10.41	13.96	14.16	12.68	12.03	11.95
ui[a]	0.1769	0.1563	0.09215	0.1479	0.04447	0.07838
error[b]	1.953	1.120	0.6510	1.166	0.3697	0.6561

[a]Uncertainty interval in the numerical estimation of kla. [b]The percentage of ui to the estimated kla value.

$$\frac{d[Ni_2P]_{sol}}{dt} = k_3 \cdot [H_2PO_2^-]_{ads}[Ni^{2+}]_{ads}^2 \quad (16)$$

$$\frac{d[Ni]_{sol}}{dt} = k_2 \cdot [Ni^{2+}]_{ads} \quad (17)$$

where $[H_2PO_2^-]$, $[Ni^{2+}]$, $[H_2PO_3^-]$, $[Ni_2P]$, and $[Ni]$ indicate the molar concentrations of the hypophosphite anion, nickel cation, phosphite anion, nickel phosphide, and metallic nickel, respectively. The subscripts "liq", "sol", and "ads" indicate the liquid phase, solid phase, and adsorbed species, while V_{sol} and V_{liq} are the volumes of the solid phase (plated layer) and the liquid phase (plating solution), respectively.

3.4. Model Fitting and Parameters. First, six parameters (kla, K_{ad1}, K_{ad2}, k_1, k_2, and k_3) are estimated for the experimental data collected at P = 30 MPa (data points = 36), the lowest pressure at which the evolution of hydrogen bubbles was suppressed. Then, one parameter (kla) is estimated for the other experimental data collected under pressures of P = 0, 50, 100, 150, and 200 MPa (the number of data points is 36 for each) using the MATLAB nonlinear least square solver function "lsqnonlin" with the trust-region-reflective algorithm (the stopping criteria 10^{-6} is included in the algorithm by default). This minimizes an objective function based on an input vector of the difference between the measured and calculated data. The uncertainty interval (ui) of each parameter vector ($\boldsymbol{p}$) is determined from the standard calculation method assuming that errors in the data are normally distributed and bearing in mind the nonlinearity of this model. The lsqnonlin Jacobian output matrix, J, is used to calculate the Hessian matrix as expressed by eq 18.

$$H = J^T J \quad (18)$$

The Hessian matrix diagonal is used to calculate the standard error, se(p_i), for parameter p_i by eq 19 with the residue of the sum of the errors squared, the number of data points (n_d) and the number of parameters (n_p).

$$se(p_i) = \sqrt{\frac{\text{residue}\ (H^T)_{ii}}{(n_d - n_p)}} \quad (19)$$

From eq 19 and the student variable, $s_{n_d - n_p}$, which gives the statistical significance of each parameter, the uncertainty interval of each parameter can be calculated according to eq 20.[26]

$$ui = \pm se(p_i) s_{n_d - n_p} \quad (20)$$

4. RESULTS AND DISCUSSION

4.1. Parameters Estimated with the Kinetic Model. The estimated parameters and associated uncertainty intervals are summarized in Table 4. kla was revealed to be the most sensitive of the six parameters involved in the kinetic model. The estimated parameter kla is estimated with high accuracy, while the adsorption coefficients (K_{ad1} and K_{ad2}) are estimated with low accuracy. The experiments are very sensitive to kla but few to adsorption coefficients, which means that the adsorption/desorption is not the rate-determining step. For experimental data obtained at other pressures, K_{ad1}, K_{ad2}, k_1, k_2, and k_3 were fixed and only kla was estimated. Under the assumption that the idea of the Hatta number (Ha), which had been applied to consider the gas−liquid mass transfer in a gas absorption system,[22] was applicable to the system (liquid−solid mass transfer) of this study also, the number could be estimated as Ha = 3.4×10^{-5} based on the values of, for example, kla = 13.96 s^{-1} and $k_1 = 4.657 \times 10^{-4}$ s^{-1}. Hence, it can be considered that the plating reaction is the rate-determining step of the mass transfer around the SLI and that the effect of the reaction on the concentration distribution in the liquid film shown in Figure 2 is negligible. The values of kla and associated uncertainty intervals are shown in Table 5. For all experiments, the residue of numerical optimization and the correlation coefficient between the calculated results with experimental data are given in Table 6.

4.2. Electroless Nickel−Phosphorus Plating. The transient changes in both the thickness of the plated layer and the concentration of the chemical species contained in the plating solution were measured and also calculated numerically by solving the mass balance equations between the chemical species in the plating solution. Figure 4 shows experimental and

Table 6. Residue in the Numerical Optimization of the Parameters and Determination Coefficient between the Calculated Results with Experimental Data

P (MPa)	residue (−)[a]	R^2 (−)[b]
0	0.02231	0.9937
30	0.005354	0.9878
50	0.001382	0.9962
100	0.005644	0.9943
150	0.005906	0.992
200	0.006491	0.9959

[a]Residue as a result of nonlinear least square method. [b]Determination coefficient.

https://dx.doi.org/10.1021/acsomega.0c00312
ACS Omega 2020, 5, 6937−6946

calculated transient changes in the thickness of the plated layer under different pressures.

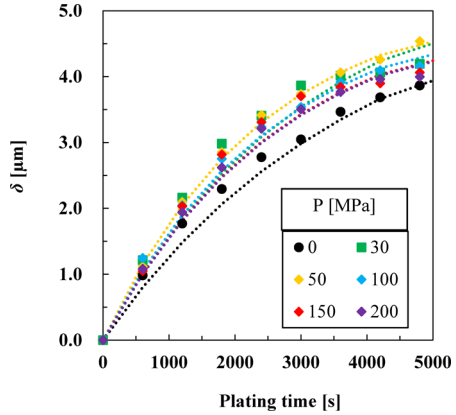

Figure 4. Transient changes of the thickness of the plated layer prepared under the different pressures, symbol: experimental data, dashed line: calculated result.

As depicted in Figure 4, the thickness of the plated layer steadily increases with time. Since the plating reaction examined in this study is a batch reaction, the transient change in the thickness of the plated layer becomes small with the progress of the reaction. It is found that growth of the plated layer terminates at about 5000 s when almost all the hypophosphite anion is consumed. It is evident that the growth of the plated layer under the condition of $P \geq 30$ MPa is faster than that for $P = 0$ MPa. It should be noted that the growth of the plated layer shows a unique dependency on the added pressure. The fastest growth is seen at $P = 50$ MPa. As can be confirmed from Figure 5, the average plating rate under the condition of $P = 50$ MPa is

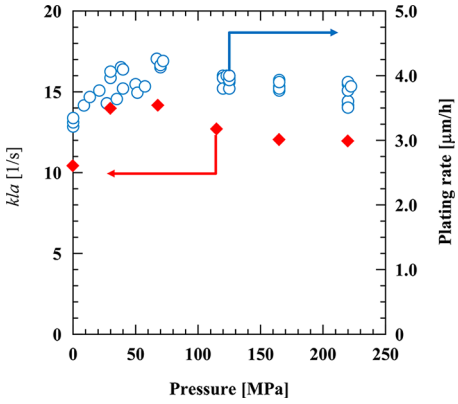

Figure 5. Effect of pressure during the plating reaction on *kla* (left axis) and plating rate (right axis).

approximately 20% greater than that for $P = 0$ MPa. These results can be explained by the following two conflicting effects: (i) suppression of the evolution of hydrogen bubbles at $P \geq 30$ MPa, and (ii) higher viscosity of the plating solution with increased P in the range of $P \geq 50$ MPa. The absence of hydrogen bubbles at the SLI facilitates mass transfer of the reaction components, resulting in accelerated growth of the plated layer. Moreover, raising the pressure eliminates hydrogen bubble formation and, as a consequence, reduces defects in the plated layer surface. It follows that this provides an effective method to improve corrosion resistivity, which is different to the methods tested in previous studies.[15,27] On the other hand, the increase in the viscosity of the plating solution appears to slow the growth of the plated layer. The effect of pressure on the viscosity of liquid can be explained by the natural convection equation on a vertical flat plate.

With regard to mass transfer by natural convection on a vertical flat plate, the three dimensionless numbers, i.e., the Sherwood number (Sh), the Grashof number (Gr), and the Schmidt number (Sc), are defined by the following eqs 21−24

$$\mathrm{Sh} = 0.59\,(\mathrm{GrSc})^{1/4} \tag{21}$$

and

$$\mathrm{Sh} = \frac{klL}{D} \tag{22}$$

$$\mathrm{Gr} = \frac{g\beta\rho^2\Delta cL}{\mu^2} \tag{23}$$

$$\mathrm{Sc} = \frac{\mu}{\rho D} \tag{24}$$

where Δc, D, g, kl, L, β, μ, and ρ are, respectively, the difference in concentration, diffusion coefficient, acceleration of gravity, mass transfer coefficient, characteristic length, coefficient of thermal expansion, viscosity of the solution, and density of the solution. Viscosity of a solution depends not only on pressure but also on the composition.[28] Because the concentrations of the chemical species contained in the plating solution, which is employed in this study, are low as summarized in Table 1, it is assumed that the viscosity of the solution is equal to that of water. By combining the eqs 21−24, we have derived the following eq 25, which indicates that the increase in the viscosity of the solution results in the decrease in the mass transfer at the SLI[28]

$$kl = \alpha\frac{1}{\mu} \tag{25}$$

where α (Pa·m) is the constant. A range of empirical equations are available to estimate water viscosity under the different temperatures and pressures.[28−30] Eq 26 was selected as it allows water viscosity to be predicted to within 3% under the experimental conditions examined in this study[29]

$$\bar{\mu} = \bar{\mu}_0(\bar{T}) \times \bar{\mu}_1(\bar{T}, \bar{\rho}) \times \bar{\mu}_2(\bar{T}, \bar{\rho}) \tag{26}$$

where the first factor $\bar{\mu}_0(\bar{T})$ depends only on temperature, the second factor $\bar{\mu}_1(\bar{T},\bar{\rho})$ represents the density contribution, while the third factor $\bar{\mu}_2(\bar{T},\bar{\rho})$ represents the enhancement of the viscosity near the critical point. The variables in the eq 27 are dimensionless as follows[29]

$$\bar{T} = \frac{T}{T_c};\ \bar{\rho} = \frac{\rho}{\rho_c};\ \bar{\mu} = \frac{\mu}{\mu_c} \tag{27}$$

The methods used to determine the above factors were previously reported.[29] To predict the density of water in the range smaller than $0.5\rho_c$, as expressed by the eq 28, the simplified form of the Virial equation is derived by truncating after the third term[30]

$$\frac{P}{\rho RT} = 1 + \beta(T)\rho + C(T)\rho^2 \tag{28}$$

where P, ρ, R, and T are pressure, the density of water, the specific gas constant, and temperature, respectively. The Virial

https://dx.doi.org/10.1021/acsomega.0c00312
ACS Omega 2020, 5, 6937−6946

coefficients in eq 28 are $\beta(T) = -1.705 \times 10^{-2}$ $m^3 \cdot kg^{-1}$ and $C(T) = 1.639 \times 10^{-5}$ $m^6 \cdot kg^{-2}$, respectively, determined from literature data.[31] The average error in the estimation of density using eq 28 is below 0.25%. Under the experimental conditions ($\overline{\rho} < 0.5$) examined in this study, it can be assumed

$$\overline{\mu_2}(\overline{T}, \overline{\rho}) = 1 \tag{29}$$

By employing the physical properties of water[29] summarized in Table 7, the relation between pressures in the range from 0 to 200 MPa with the viscosity of water is derived as shown in Figure 6. The average errors in the estimation of water viscosity by an IAPWS model[29] and our viscosity model are 3 and 3.4%, respectively. The main difference between the two models comes from the Virial coefficient values. Some experimental values[32] are added to Figure 6 to show the accuracy of the employed model. The calculated result and experimental data are in good agreement. The average error in the experimental values is only 0.7% according to the literature.[31] The employed model is thus validated.

Table 7. Physical Properties of Water[29]

ρ_c ($kg \cdot m^{-3}$)	322.0
T_c (K)	647.096
p_c (MPa)	22.064
μ_c (Pa·s)	1.0×10^{-6}
R ($kJ \cdot kg^{-1} \cdot K^{-1}$)	0.46151805

4.3. Results of Simulation and Comparison with Experimental Data. Based on our proposed kinetic model taking into account both the mass transfer and the chemical reactions in the vicinity of the growing surface of the plated layer, the transient changes of the thickness of the plated layer and the concentrations of the reaction components were simulated. As far as the authors have investigated, to date, with regard to the mechanism of the ENPP, the growth of the plated layer has not yet been discussed based on the mass balance equations between the reaction components. It is evident that the greater growth rate of the plated layer is the result of the greater consumption rate of the reaction components, such as the hypophosphite anion and nickel cation. The volumetric mass transfer coefficient *kla* (Figure 5) was numerically estimated by fitting the calculated thickness of the plated layer (Figure 4) and the concentration of the chemical species to the experimental data, which was measured under a different value of P (Figure 7). In the numerical optimization to ascertain the solution of the parameters, it was confirmed, as summarized in Table 5, that the error was sufficiently small. As depicted in Figure 5, it should be noted that *kla* reached a peak under the condition of $P = 50$ MPa in the examined range from 0 to 200 MPa. The dependence of *kla* on pressure (left axis) is quite similar to that of the plating rate (right axis) as also depicted in Figure 5. The mass transfer coefficient, *kl*, can be estimated by dividing *kla* with the effective surface-to-volume ratio, a ($m^2 \cdot m^{-3}$). Considering the thickness of the substrate, the values of a were determined as 6.67×10^3 $m^2 \cdot m^{-3}$ for cases with no bubble and 5.8×10^3 $m^2 \cdot m^{-3}$ for cases with a bubble, respectively. By applying eq 25 to thus attained *kl* and μ, which was estimated from the relation shown in Figure 6, the constant α in eq 25 could be determined as $\alpha = 8.56 \times 10^{-7}$ Pa·m. Using the six parameters determined using the nonlinear least square method, the transient changes in the thickness of the plated layer and the concentration of the chemical species were calculated. Figures 4 and 7a–c show that the calculated results closely coincided with the experimental data, with the determination coefficients being mostly over 99% as summarized in Table 6.

The deviations of the calculated results from the experimental data in Figure 7 could be explained in terms of the limitation of LDF approximation for ionic systems. Although the electrical charge density was assumed to be equal to zero, the small discrepancy observed in Figure 3 could explain the deviations of the Figure 7. Indeed, Grimes and Liapis[33] have shown that the electrophoretic mass transport due to electrical charge density can have a strong influence on total ionic species transport in the liquid film. To fit the calculated result to the experimental data in Figure 7 with higher accuracy, it could be necessary to consider

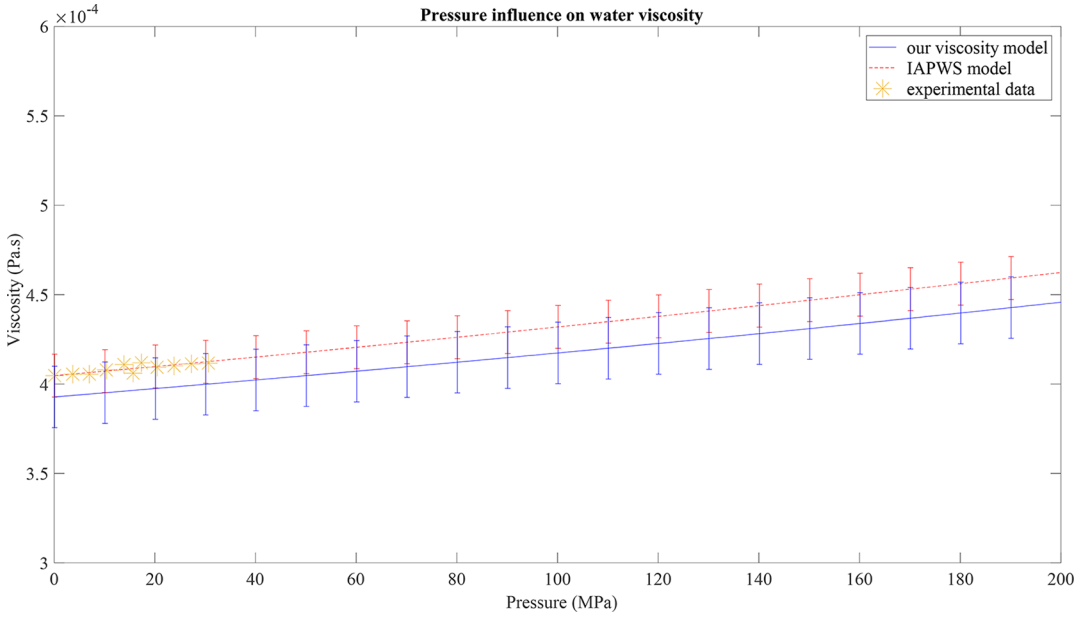

Figure 6. Relation between pressure and water viscosity, red dashed line: IAPWS model calculated result, blue solid line: our viscosity model, dots: experimental viscosity data at 343 K.

https://dx.doi.org/10.1021/acsomega.0c00312
ACS Omega 2020, 5, 6937–6946

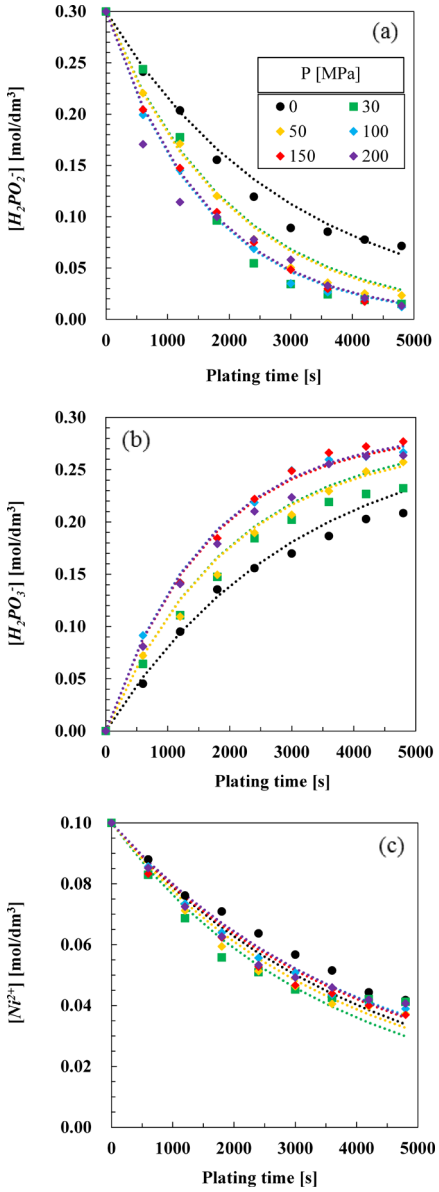

Figure 7. Transient changes of (a) $[H_2PO_2^-]$, (b) $[H_2PO_3^-]$, and (c) $[Ni^{2+}]$ under the different plating pressures, dashed line: calculated result, solid symbol: experimental data.

the electrophoretic mass transport of the different ionic species in the kinetic model.[33]

5. CONCLUSIONS

Electroless nickel−phosphorus plating (ENPP) under high pressure is a novel and effective method for suppressing the evolution of hydrogen bubbles during the plating reaction under ambient pressure and which may cause defects such as pinholes or nodules in the plated layer. In this study, we examined the effects of high pressure on the formation of the plated layer based on the mass balance equations of the chemical species relevant to the evolution of hydrogen. To simulate the plating reaction, we developed a kinetic model that took into account both mass transfer and the reactions of the chemical species on the growing surface of the plated layer or the solid−liquid interface (SLI). By fitting the simulated results to the experimental ones, based on the nonlinear least square method, we were able to determine the mass transfer coefficient or *kla* of the chemical species at the SLI. As a result, we confirmed that the kinetic model can account for the two conflicting effects of high pressure on ENPP: (i) acceleration of mass transfer as a result of the suppression of hydrogen bubbles, and (ii) deceleration of mass transfer as a result of the higher viscosity of the plating solution. Using our determined *kla*, we numerically calculated the transient changes in the thickness of the plated layer and the concentrations of the chemical species. These were very similar to the experimental data. In a subsequent study, we will examine the effects of pressure on the adsorption kinetics of the chemical species on the SLI in our proposed model. The applicability of the model to the other plating processes will also be studied.

AUTHOR INFORMATION

Corresponding Author

Takuji Yamamoto − *Department of Chemical Engineering and Materials Science, Graduate School of Engineering, University of Hyogo, Himeji 671-2280, Japan;* orcid.org/0000-0002-6720-6789; Phone: +81-79-267-4849; Email: tyamamot@eng.u-hyogo.ac.jp

Authors

Hirotaka Yokohama − *Department of Chemical Engineering and Materials Science, Graduate School of Engineering, University of Hyogo, Himeji 671-2280, Japan*

Mélaz Tayakout-Fayolle − *Laboratoire d'Automatique, de génie des Procédés et de génie Pharmaceutique (LAGEPP), Université Claude Bernard Lyon 1, Villeurbanne F-69100, France;* orcid.org/0000-0002-0667-3535

Aurélie Galfré − *Laboratoire d'Automatique, de génie des Procédés et de génie Pharmaceutique (LAGEPP), Université Claude Bernard Lyon 1, Villeurbanne F-69100, France*

Naoki Fukumuro − *Department of Chemical Engineering and Materials Science, Graduate School of Engineering, University of Hyogo, Himeji 671-2280, Japan*

Shinji Yae − *Department of Chemical Engineering and Materials Science, Graduate School of Engineering, University of Hyogo, Himeji 671-2280, Japan*

Kouji Maeda − *Department of Chemical Engineering and Materials Science, Graduate School of Engineering, University of Hyogo, Himeji 671-2280, Japan*

Complete contact information is available at: https://pubs.acs.org/10.1021/acsomega.0c00312

Notes

The authors declare no competing financial interest.

ACKNOWLEDGMENTS

The authors thank Y. Yasui for her technical assistance to observe hydrogen bubbles.

NOMENCLATURE

a	the effective surface-to-volume ratio ($m^2 \cdot m^{-3}$)
A	the surface area of copper piece (m^2)
Δc	the difference of concentration ($mol \cdot m^{-3}$)
D	the diffusion coefficient ($m^2 \cdot s^{-1}$)
g	the acceleration of gravity ($m \cdot s^{-2}$)
Gr	the Grashof number (−)
Ha	the Hatta number (−)
$[H_2PO_2^-]$	the molar concentrations of the hypophosphite anion ($mol \cdot dm^{-3}$)

https://dx.doi.org/10.1021/acsomega.0c00312
ACS Omega 2020, 5, 6937−6946

$[H_2PO_3^-]$	the molar concentrations of the phosphite anion ($mol·dm^{-3}$)
K_{ad1}	the adsorption constant of $H_2PO_2^-$ on SLI (−)
K_{ad2}	the adsorption constant of Ni^{2+} on SLI (−)
kla	the volumetric mass transfer coefficient of the chemical species in the liquid film (s^{-1})
kl	the mass transfer coefficient of the chemical species in the liquid film ($m·s^{-1}$)
k_1	the reaction rate constant of the eq 2 (s^{-1})
k_2	the reaction rate constant of the eq 3 (s^{-1})
k_3	the reaction rate constant of the eq 4 ($dm^6·mol^{-2}·s^{-1}$)
L	the characteristic length (m)
M_1	the weight of copper piece after plating (kg)
M_2	the weight of copper piece before plating (kg)
[Ni]	the molar concentrations of metallic nickel ($mol·dm^{-3}$)
$[Ni^{2+}]$	the molar concentrations of the nickel cation ($mol·dm^{-3}$)
$[Ni_2P]$	the molar concentrations of nickel phosphide ($mol·dm^{-3}$)
P	pressure (MPa)
p_c	the critical pressure of water (MPa)
R	the specific gas constant ($kJ·kg^{-1}·K^{-1}$)
R^2	determination coefficient (−)
Sc	the Schmidt number (−)
Sh	the Sherwood number (−)
T_c	the critical temperature of water (K)
V_{sol}	the volumes of the solid phase (plated layer) (dm^3)
V_{liq}	the volumes of the liquid phase (plating solution) (dm^3)
z	ion charge (−)

Subscripts

ads	adsorbed species
liq	liquid phase
sol	solid phase

Superscript

int	interface

Greek letters

β	the coefficient of thermal expansion ($m^3·mol^{-1}$)
δ	the thickness of the plated layer (μm)
λ	ionic equivalent conductivity ($S·m^2·mol^{-1}$)
μ	the viscosity of the solution (Pa·s)
μ_c	the critical viscosity of water (Pa·s)
ρ	the average density of the plated layer ($kg·m^{-3}$)
ρ_c	the critical density of water ($kg·m^{-3}$)

REFERENCES

(1) Archibald, P. Isostatic solvent pressing. *Ind. Eng. Chem. Res.* **1961**, *53*, 737−738.

(2) Li, S.; Qi, H.; Xu, N.; Shi, J. Tubular dense perovskite type membranes. preparation, sealing, and oxygen permeation properties. *Ind. Eng. Chem. Res.* **1999**, *38*, 5028−5033.

(3) Chard, W.; Conaway, M.; Niesz, D. Advanced high pressure graphite processing technology. *ACS Symp. Ser.* **1976**, *21*, 155−171.

(4) Bazargan, A.; Yan, Y.; Hui, C. W.; McKay, G. A Review: Synthesis of carbon-based nano and micro materials by high temperature and high pressure. *Ind. Eng. Chem. Res.* **2013**, *52*, 12689−12702.

(5) Mandal, M.; Landskron, K. Synthetic chemistry with periodic mesostructures at high pressure. *Acc. Chem. Res.* **2013**, *46*, 2536−2544.

(6) Li, H.; Su, L.; Zhu, X.; Cheng, X.; Yang, K.; Yang, G. In situ crystallization of ionic liquid [Emim][PF_6] from methanol solution under high pressure. *J. Phys. Chem. B* **2014**, *118*, 8684−8690.

(7) Yoshino, T.; Maruyama, K.; Kagi, H.; Nara, M.; Kim, J. C. Pressure-induced crystallization from amorphous calcium carbonate. *Cryst. Growth Des.* **2012**, *12*, 3357−3361.

(8) Moritoki, M.; Nishiguchi, N.; Nishida, S. Features of the high-pressure crystallization process in industrial use. *ACS Symp. Ser.* **1997**, *667*, 136−149.

(9) Krulik, G. A. Electroless plating of plastics. *J. Chem. Educ.* **1978**, *55*, 361−365.

(10) Dinderman, M. A.; Dressick, W. J.; Kostelansky, C. N.; Price, R. R.; Qadri, B. S.; Schoen, E. P. Electroless plating of iron onto cellulose fibers. *Chem. Mater.* **2006**, *18*, 4361−4368.

(11) Pernstich, K. P.; Schenker, M.; Weibel, F.; Rossi, A.; Caseri, W. R. Electroless plating of ultrathin films and mirrors of platinum nanoparticles onto polymers, metals, and ceramics. *ACS Appl. Mater. Interfaces* **2010**, *2*, 639−643.

(12) Brenner, A.; Riddel, G. E. Nickel plating on steel by chemical reduction. *J. Res. Natl. Bur. Stan.* **1946**, *37*, 31−34.

(13) Qi, Z.; Lu, W.; Guo, A.; Hu, Y.; Lee, W.; Zhang, X. Investigation on circular plating pit of electroless Ni−P coating. *Ind. Eng. Chem. Res.* **2014**, *53*, 3097−3104.

(14) Nwosu, N.; Davidson, A.; Hindle, C.; Barker, M. On the influence of surfactant incorporation during electroless nickel plating. *Ind. Eng. Chem. Res.* **2012**, *51*, 5635−5644.

(15) Chen, B.-H.; Hong, L.; Ma, Y.; Ko, T.-M. Effects of surfactants in an electroless nickel-plating bath on the properties of Ni−P alloy deposits. *Ind. Eng. Chem. Res.* **2002**, *41*, 2668−2678.

(16) Kunimoto, M.; Homma, T. Research trends in electroless plating process. *J. Surf. Finish. Soc. Jpn* **2015**, *66*, 438−442.

(17) Nobuyoshi, Y.; Yamamoto, T.; Maeda, K.; Fukumuro, N.; Yae, S. Electroless nickel-phosphorus plating under high pressurec. *Kagaku Kogaku Ronbunshu Jpn.* **2018**, *44*, 1−4.

(18) Nguyen, M.-T.; Tayakout-Fayolle, M.; Pirngruber, G. D.; Chainet, F.; Geantet, C. Kinetic modeling of quinoline hydro-denitrogenation over a NiMo(P)/Al_2O_3 catalyst in a batch reactor. *Ind. Eng. Chem. Res.* **2015**, *54*, 9278−9288.

(19) Lordgooei, M.; Sagen, J.; Rood, M. J.; Rostam-Abadi, M. Sorption and modeling of mass transfer of toxic chemical vapors in activated-carbon fiber-cloth adsorbers. *Energy Fuels* **1998**, *12*, 1079−1088.

(20) Kovalchuk, K.; Riccardi, E.; Grimes, B. A. Multiscale modeling of mass transfer and adsorption in liquid−liquid dispersions. 2. application to calcium naphthenate precipitation in oils containing mono- and tetracarboxylic acids. *Ind. Eng. Chem. Res.* **2014**, *53*, 11704−11719.

(21) Marton, J. P.; Schlesinger, M. The nucleation, growth, and structure of thin Ni-P films. *J. Electrochem. Soc.* **1968**, *115*, 16−21.

(22) Bird, R. B.; Stewart, W. E.; Lightfoot, E. N. *Transport Phenomena*; 2nd ed.; Wiley: New York, 1960; pp 513−515, 695−697.

(23) Smith, R. S.; Martell, A. E. *Critical Stability Constants*; Springer: Boston, MA, 1989, pp 1−619.

(24) Newman, J.; Thomas-Alyea, K. E. *Electrochemical Systems; 3rd ed.*; Wiley: New Jersey, 2004, pp. 1−672.

(25) Meites, L. *Handbook of Analytical Chemistry*; New York: McGraw-Hill, 1963, pp.1−1806.

(26) Couenne, F.; Jallut, C.; Tayakout-Fayolle, M. On minimal representation of heterogeneous mass transfer for simulation and parameter estimation: application to breakthrough curves exploitation. *Comput. Chem. Eng.* **2005**, *30*, 42−53.

(27) Chen, C.-H.; Chen, B.-H.; Hong, L. Role of Cu^{2+} as an Additive in an Electroless Nickel−Phosphorus Plating System; A Stabilizer or a Codeposit? *Chem. Mater.* **2006**, *18*, 2959−2968.

(28) Poling, B. E.; Prausnitz, J. M.; O' Connell, J. *The Properties of Gases and Liquids; 5th ed.*; McGraw-Hill: New York, 2000, pp. 1−701.

(29) Huber, M. L.; Perkins, R. A.; Laesecke, A. R.; Friend, D. G.; Sengers, J. V.; Assael, M. J.; Metaxa, I. N.; Vogel, E.; Mareš, R.; Miyagawa, K. New International Formulation for the Viscosity of H_2O. *J. Phys. & Chem. Ref. Data* **2009**, *38*, 101−125.

(30) Wagner, W.; Pruß, A. The IAPWS Formulation 1995 for the Thermodynamic Properties of Ordinary Water Substance for General and Scientific Use. *J. Phys. & Chem. Ref. Data* **2002**, *31*, 387−535.

https://dx.doi.org/10.1021/acsomega.0c00312
ACS Omega 2020, 5, 6937−6946

(31) Kell, G. S.; Whalley, E. Reanalysis of the Density of Liquid Water in the Range 0−150 °C and 0−1 kbar. *J. Chem. Phys.* **1975**, *62*, 3496−3503.
(32) Kestin, J.; Shankland, J. R. The Free Disk as an Absolute Viscometer and the Viscosity of Water in the Range 25−150°C. *J. Non-Equil. Thermodyn.* **1981**, *6*, 241−256.
(33) Grimes, B. A.; Liapis, A. I. The Interplay of Diffusional and Electrophoretic Transport Mechanisms of Charged Solutes in the Liquid Film Surrounding Charged Nonporous Adsorbent Particles Employed in Finite Bath Adsorption Systems. *J. Colloid Interface Sci.* **2002**, *248*, 504−520.

https://dx.doi.org/10.1021/acsomega.0c00312
ACS Omega 2020, 5, 6937−6946